WELDING RESEARCH

SUPPLEMENT TO THE *WELDING JOURNAL*, October 2000
**Sponsored by the American Welding Society and the Welding Research Council**



# Nature and Evolution of the Fusion Boundary in Ferritic-Austenitic Dissimilar Metal Welds — Part 2: On-Cooling Transformations

*On-cooling transformations in the fusion zone and heat-affected zone were studied for their relation to crack initiation*

**BY T. W. NELSON, J. C. LIPPOLD AND M. J. MILLS**

ABSTRACT. Microstructural evolution at the fusion boundary in dissimilar welds between ferritic and austenitic alloys can significantly influence both the weldability and service behavior of the dissimilar combination. A fundamental investigation was undertaken to characterize fusion boundary microstructure and to better understand the nature and character of boundaries that are associated with cracking in dissimilar welds. In a previous paper, the evolution of the fusion boundary during the onset of solidification was discussed. In this paper, the nature and evolution of the fusion boundary and surrounding regions in dissimilar metal welds during subsequent on-cooling transformations in the fusion zone and heat-affected zone (HAZ) will be discussed.

A model system consisting of a high-purity iron base metal and 70Ni-30Cu (AWS A5.14 ERNiCu-7) filler metal was used to study this behavior. Using this simple Fe-Ni-Cu system, fusion boundary microstructures were developed that were analogous to those observed in more complex engineering systems. Transmission electron diffraction analysis and orientation imaging microscopy (OIM) revealed the orientation relationships between adjacent HAZ and weld metal grains at the fusion boundary were different than the cube-on-cube relationship normally observed in similar metal welds. The room temperature fusion boundary in the system studied exhibited grain boundary misorientations consistent with common FCC/BCC relationships, *i.e.,* Bain, Kurdjumov-Sachs and Nishyama-Wassermann. A theory describing the evolution of the fusion boundary is proposed and the nature and character of the "Type II" grain boundary is described.

*T. W. NELSON, formerly with The Ohio State University, is now with Brigham Young University in Provo, Utah. J. C. LIPPOLD and M. J. MILLS are with The Ohio State University, Columbus, Ohio.*

## Introduction

Cracking phenomena associated with welds have been a recurring problem that has received considerable attention by many researchers over the last four decades. It is well accepted that weld-related cracking normally occurs along grain boundaries. Such grain-boundary-related cracking phenomena include weld solidification cracking, weld metal liquation cracking (microfissuring) in multipass welds, HAZ liquation cracking, reheat (stress relief) and strain-age cracking, and ductility dip cracking in both the weld metal and HAZ. Unfortunately, the materials that exhibit the greatest propensity for these cracking phenomena are those that are vital to the national infrastructure, *i.e.,* aluminum alloys, nickel-based alloys and stainless steels.

**KEY WORDS**

Dissimilar Welds
Grain Boundary
Crack Growth
On-Cooling
Phase Transformation
Ferritic-Austenitic
Weld Cracking

Cladding or dissimilar metal welds have by no means been immune to such failures and exhibit some unique cracking phenomena not observed in welds between similar materials. In fact, cracking or disbonding along or near the fusion boundary in dissimilar ferritic-austenitic welds has been a persistent problem for more than 60 years. Despite the persistence and potential consequences, the evolution, nature and role of weld metal interfaces in promoting or mitigating weld-related cracking are not well understood. The implications of boundaries and structures with regard to crack growth rates, fatigue, stress corrosion cracking, etc., have been researched extensively in the materials science arena. However, in spite of the recurring problems and economic losses, there exists a lack of understanding regarding the role of boundaries and structures in promoting or mitigating weld-related cracking. Therefore, a fundamental investigation was undertaken to investigate the nature and character of those boundaries and structures near the fusion boundary in dissimilar ferritic-austenitic welds.

A previous paper (Ref. 1) addressed the nature and character of the elevated temperature fusion boundary at the onset of solidification. This paper will present in detail the effects of on-cooling transformations and the nature of the fusion boundary and surrounding microstructure within the austenitic and alpha ferrite temperature ranges.

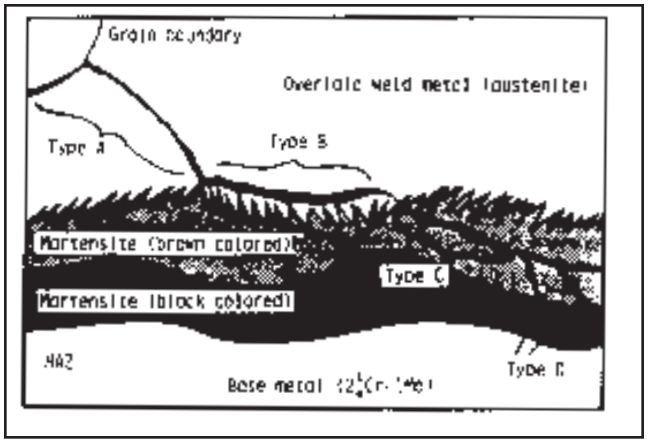


*Fig. 1 — Schematic representation of fusion boundary morphologies observed in DMWs (Ref. 1).*

## Background

Despite the widespread application of dissimilar metal joining, there is a history of weld-related failures associated with dissimilar joints. In the power generation industry, dissimilar welding or cladding is used in nuclear steam generator channel heads, pressurized water reactors, tube sheets and reheat piping. Cladding in these applications is primarily used as an erosion/corrosion inhibitor in an elevated-temperature, high-velocity steam environment. The petrochemical industry also utilizes dissimilar welding/cladding for similar benefits. Cladding with austenitic stainless steel for corrosion resistance is used extensively in hydro-desulfurization reactors and other pressure vessels (Refs. 2–13). For these particular applications, austenitic stainless steels or nickel-based alloys are clad onto a carbon or Cr-Mo steel substrate to inhibit corrosion and high-temperature oxidation, save material costs and prolong the life of the component. However, in some instances, these weld claddings have failed catastrophically near the weld fusion boundary. Failures such as these cost industry millions of dollars each year in repair or replacement (Refs. 14, 15).

Research activities and reported failures associated with DMW date back to the early 1930s (Refs. 14, 15). Of the failures reported, whether produced in the laboratory or in actual fabrications, cracking has been observed in several locations near the fusion boundary region. These locations include 1) the weld fusion boundary, 2) the weld heat-affected zone, and 3) grain boundaries in the weld metal oriented parallel to the fusion boundary. These parallel boundaries, sometimes referred to as Type II boundaries, are shown schematically in Fig. 1, labeled Type B. Many of the failures reported occur along the Type II boundaries, which tend to be oriented parallel to the fusion boundary and less than 100 µm away from the fusion boundary. This morphology is contrary to that observed in similar metal welds, in which solidification grain boundaries are oriented roughly normal to the fusion boundary and are the extension of HAZ grain boundaries at the fusion boundary as a consequence of the epitaxial nature of solidification nucleation.

The dissimilar test sample shown in Fig. 2 was made on ASTM A508 base metal, clad with Type 309L stainless steel on the first pass, followed by Type 308L stainless steel on the second pass, and subsequent passes with AWS ENiCrFe-3. Shielded metal arc welding (SMAW) was used as the welding process in this test sample. In this figure, the Type II boundaries can be seen running roughly parallel to the fusion boundary. This morphology is unconventional relative to similar material combinations and has shown to have important implications with respect to both fabricability and structural integrity. From Fig. 3, it can be observed that the fracture path follows along the Type II boundary. This is the fracture path observed by many investigators (Refs. 2–4) when investigating clad disbonding.

Much of the research to date has investigated the effect of hydrogen on Type II boundary failure or implicated hydrogen-induced cracking as part of the mechanism (Refs. 2–15). Most of these investigations have been successful at promoting cracking in dissimilar metal welds by cathodically charging samples to very high hydrogen concentrations. However, some have proposed that it is the very high pressures that promote cracking in these investigations, and that hydrogen, although a contributor, is not the underlying mechanism (Ref. 8). Other instances of Type II boundary cracking cannot be related to hydrogen-induced cracking because of the absence of hydrogen in the fabrication or service environment. Although considerable work has attempted to determine the underlying mechanisms responsible for this form of weld cracking, little research has focused on understanding the nature and evolution of those weld metal interfaces along which cracking occurs.

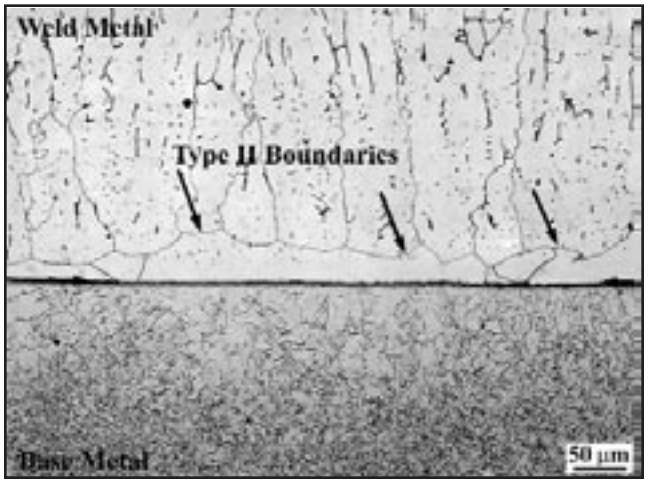


*Fig. 2 — Weld metal microstructure in clad component.*

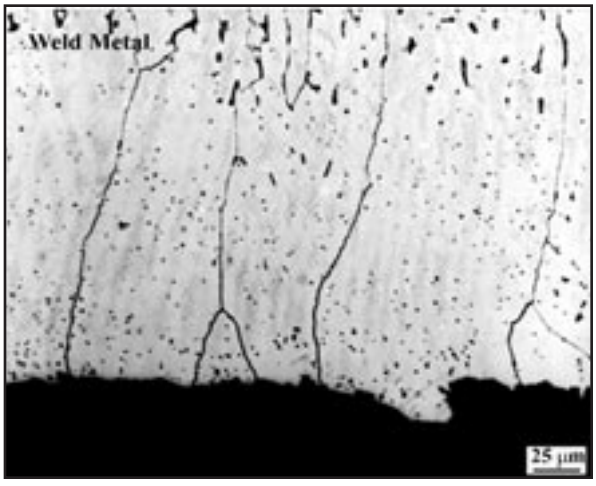


*Fig. 3 — Fracture profile showing failure along Type II boundary in an actual clad test component.*

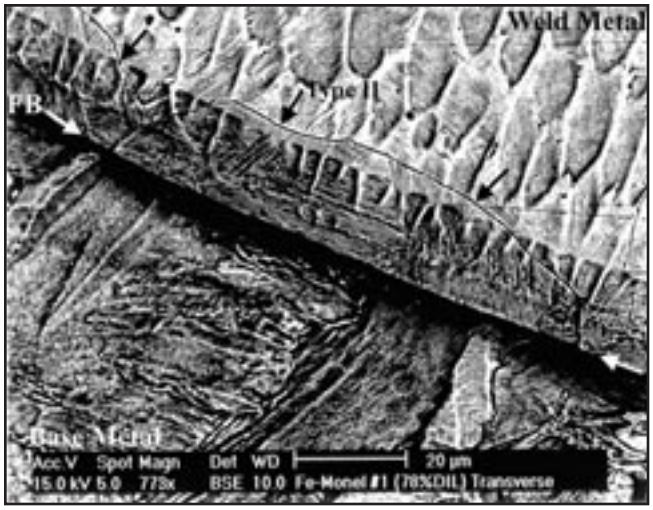


*Fig. 4 — BSE photomicrograph showing the Type II boundaries (indicated by arrows) extending beyond the martensitic transition region at the fusion boundary into the fully austenitic weld metal (65% BMD weld in Fe/70Ni-30Cu).*

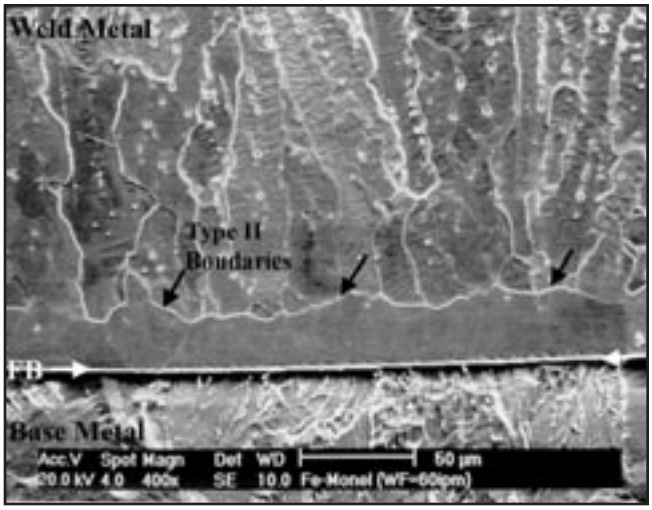


*Fig. 5 — SE photomicrograph showing Type II boundaries (indicated by arrows) running parallel to the entire fusion boundary (48% BMD weld in Fe/70Ni-30Cu).*

Although not well understood, the region of the weld near the fusion boundary has proven to have important implications on the failures associated with DMWs. It has been hypothesized (Refs. 2–16) that microstructural and chemical transitions exist from the fusion boundary across these Type II boundary regions. A number of factors support the existence of this transitional region: 1) different crystal structures between the body-centered cubic (BCC) ferritic base metal and the face-centered-cubic (FCC) weld metal; 2) diffusional mixing of alloying and impurity elements from the weld metal into a stagnant boundary layer adjacent the fusion boundary; 3) changing base metal dilution (BMD), which affects the composition gradient in the weld metal at the fusion boundary; and 4) the diffusion and growth kinetics during multipass welds and long postweld heat treatments (PWHT).

This transition region, its crystal structure and composition, can ultimately govern the ability of a welded component to be successfully fabricated and perform as engineered in its intended service environment.

Few previous investigators have addressed or proposed any mechanisms regarding the nature and evolution of the Type II boundary. Recently, one hypothesis was developed by Wu, *et al.* (Ref. 16), with regard to the formation of the Type II boundary. They proposed the Type II boundary was a result of a change in the primary mode of solidification. According to their hypothesis, primary solidification from the body-centered-cubic (BCC) substrate occurs as ferrite (BCC), and, at some distance from the fusion boundary, the mode changes to a primary austenite as a result of the increasing amount of austenite stabilizing elements toward the center of the weld. This solidification mode change would create a Type II boundary. The distance at which the change in solidification mode would occur would be governed by the slope of the composition gradient within the transition region adjacent the fusion boundary. Other than this theory, there is little information in the literature regarding the evolution of the fusion boundary in DMWs and Type II boundaries. Therefore, a fundamental investigation was undertaken to investigate the nature and character of those boundaries and structures near the fusion boundary in dissimilar metal welds.

**Table 1 — Chemical Composition of Base and Filler Metal**

| Element | Iron | ERNiCu-7 actual | ERNiCu-7 AWS A5.14 |
|---|---|---|---|
| Fe | Bal. | 0.25 | 2.5 Max |
| Ni | | 65.57 | 62.0–69.0 |
| Cu | | 27.84 | Remainder |
| Cr | | 0.015 | Not Specif. |
| C | 0.020 | 0.048 | 0.15 Max |
| Mn | 0.320 | 3.58 | 4.0 Max |
| Si | 0.010 | 0.85 | 1.25 Max |
| Ti | | 1.99 | 1.5–3.0 |
| Al | | — | 0.02 Max |
| S | 0.013 | 0.0003 | 0.015 Max |
| P | 0.010 | — | 0.02 Max |
| Nb+Ta | | 0.005 | Not Specif. |
| $Cr_{eq}$ | 0.0 | 1.3 | N/A |
| $Ni_{eq}$ | 0.8 | 68.8 | N/A |

## Experimental Approach

### Material Selection

A simple ternary system that would represent the solidification and phase transformation behavior of more complex dissimilar alloy combinations was selected for this investigation. High-purity iron was used as a base metal as it exhibits both the delta-gamma and gamma-alpha transformations that occur in C-Mn and low-alloy structural steels. A 70Ni-30Cu, single-phase (FCC) binary alloy with low impurity content was selected as the filler metal. The chemical compositions of both the base and filler metals are listed in Table 1.

### Welding Conditions

Gas tungsten arc welding (GTAW) using a cold wire and argon shielding gas was used for producing single-pass bead-on-plate welds. Current, voltage and travel speeds were held constant for all welds at 250 A, 11 V and 6 in./min (2.5 mm/s), respectively. Wire feed speed was used as the primary variable for controlling and changing the base metal dilution (BMD), where BMD defines the percent base metal composing the weld metal. Wire feed rates ranged from 10 to 100 in./min (4.2–42.3 mm/s), producing BMDs ranging from 10–80%.

### Microstructural Characterization

Numerous transverse and plan view samples were removed from welds of various BMDs for metallographic analysis. Standard metallographic techniques were used to prepare optical and scanning electron microscopy (SEM) samples. Because of the different characteristics of the base and weld metal, two etchants

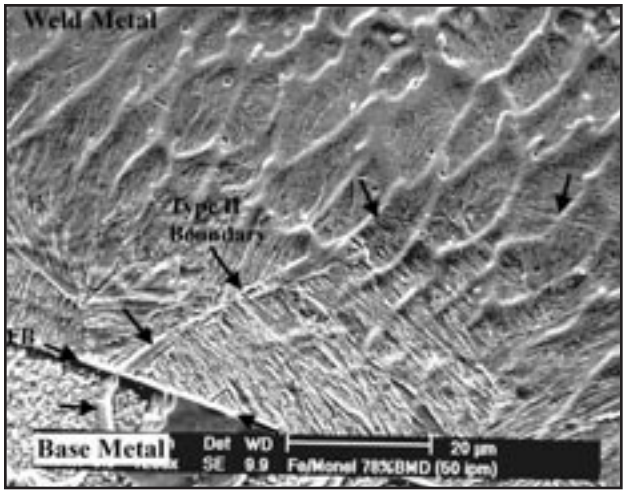


*Fig. 6 — SE micrograph showing continuity of Type II boundary (indicated by arrows) and a prior austenite HAZ grain boundary (56% BMD weld in Fe/70Ni-30Cu).*

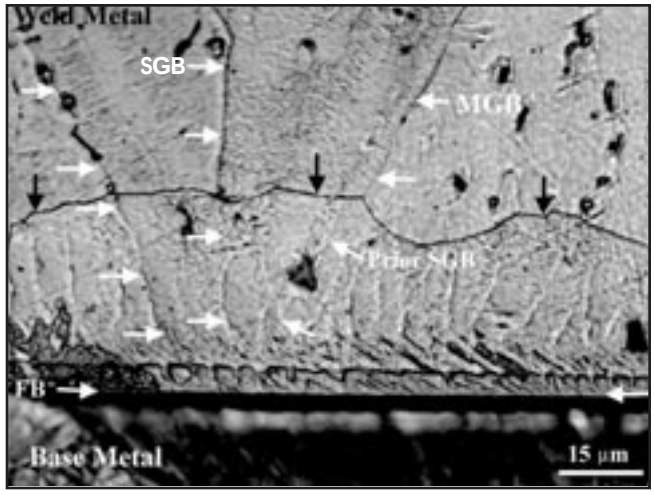


*Fig. 7 — Photomicrograph indicating evidence of prior SGBs (white arrows) that extended to the fusion boundary below the Type II boundaries (black arrows) (56% BMD weld in Fe/70Ni-30Cu).*

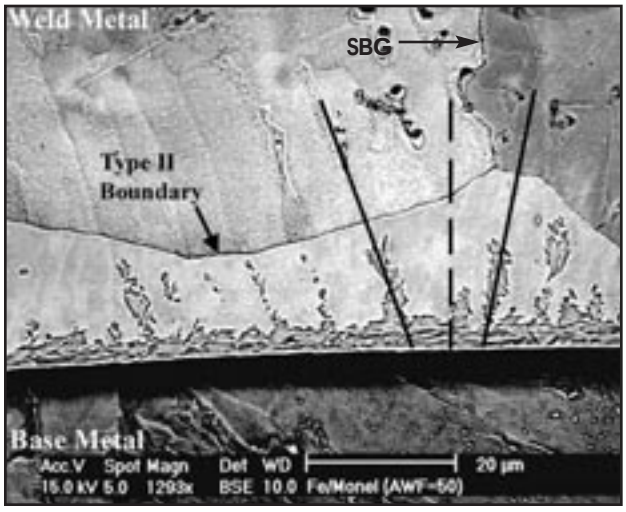


*Fig. 8 — SE photomicrograph illustrating the extension of prior SGB evident by the transformation product at the fusion boundary (56% BMD weld in Fe/70Ni-30Cu).*

were used for metallographic preparation of samples. These included 1) 4% nital, which etches the base metal; and 2) an electrolytic solution of 5 g $Fe_3Cl$, 2 mL of HCL and 99 mL of methanol for the weld metal. Optical microscopy and scanning electron microscopy (SEM) were used for microstructure characterization of structures and boundaries along the fusion boundary. Optical metallography was performed at magnifications up to 400X and SEM analysis up to 1600X.

#### Transmission Electron Microscopy Analysis

Discs were removed along the fusion boundary from transverse sections using a 3-mm-diameter disc punch. Standard grinding and dimpling techniques were utilized for reducing the thickness of the disks. Following dimpling, samples were ion milled from both sides until perforation of the foil was achieved. Transmission electron microanalysis (TEM) was performed using standard bright-field, two-beam and microdiffraction conditions (Ref. 17).

#### Electron Backscatter Analyses

Electron backscatter diffraction analyses was performed on both TEM thin foils and bulk metallographically prepared samples. Samples were loaded in the SEM at an angle of 70 deg from the incident beam toward a phosphor detector. The electron beam was then rastered across the sample in a hexagonal grid at specified increments. Kikuchi signals were automatically analyzed using the Orientation Imaging Microscopy (OIM™) software (Refs. 18–20). This software calculates the Euler angles of the electron backscatter diffraction (EBSD) patterns with reference to the sample normal, then stores the position and angles of each pattern. This data was then used for various grain boundary and texture analysis.

## Results

The ability of the base and filler metal combination used in this investigation to reproduce those microstructures commonly observed in engineering materials has been demonstrated previously (Ref. 21). The microstructures observed along the fusion boundary exhibited a fully martensitic microstructure at high BMDs (>80%), a mostly austenitic weld metal microstructure with a band of martensite along the fusion boundary at medium BMDs (80%>BMD<20%), and a fully austenitic weld metal microstructure at low BMDs (<20%). The Type II boundaries are observed in welds of various BMDs as shown in Figs. 4 and 5. Note that Type II boundaries can exist in both the martensitic and austenitic regions of the compositional transition region adjacent to the fusion boundary — Fig. 4. As BMD decreases, the amount of martensite decreases, and the Type II boundaries become more prominent. At approximately 48% BMD, there is little evidence of any martensite and the Type II boundaries are clearly evident along the entire fusion boundary — Fig. 5.

Several interesting microstructural characteristics that add insight into the evolution of the Type II boundaries were observed. In some cases, evidence of correlation between HAZ and Type II grain boundaries were observed. In Fig. 6, evidence of continuity between a prior austenite HAZ grain boundary and a Type II boundary at the fusion boundary can be observed. Another interesting characteristic of the Type II boundary is manifested by the nature of the solidification grain boundaries (SGBs) and solidification subgrain boundaries. In most cases, solidification subgrain boundaries (cell and dendrite boundaries) are clearly distinguishable despite any grain bound-

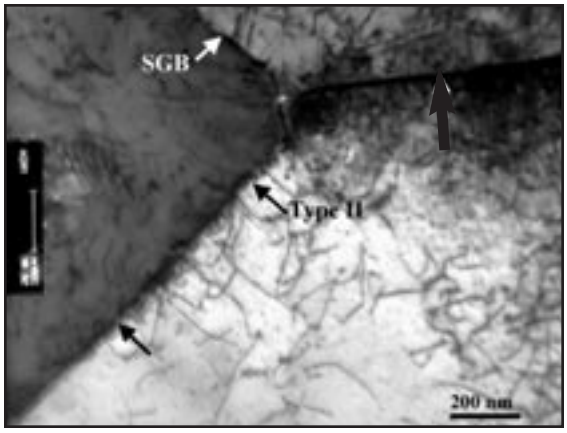


*Fig. 9 — TEM photomicrograph showing intersection of SGB (white arrow) and Type II boundary (indicated by black arrows) (48% BMD weld in Fe/70Ni-30Cu).*

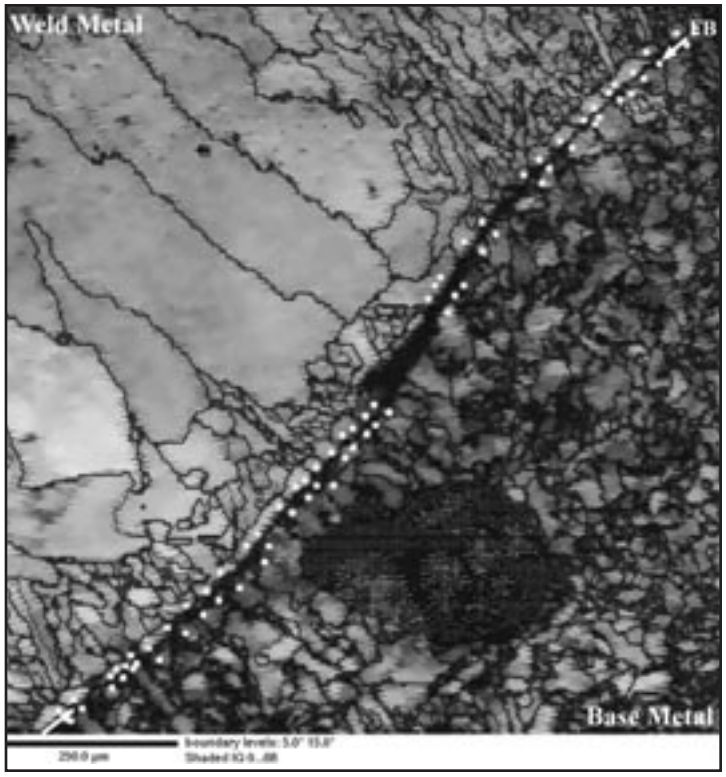


*Fig. 10 — Image quality grain map of fusion boundary region in 48% BMD weld in Fe/70Ni-30Cu. Note the Type II boundaries decorating the entire fusion boundary.*

ary migration or transformation product, as observed in Fig. 7. This is usually a result of the composition differences between the cell cores and cell boundaries that change the nature of etching or transformation between these two regions.

As mentioned previously, it seemed as if the Type II boundaries traverse several SGBs even though the solidification substructure was not evident within the Type II grains. In Figs. 7 and 8, it is evident the original SGBs extend to the fusion boundary as indicated by the arrows. Although the crystallographic portion of the SGBs, referred to as migrated grain boundaries, was eliminated by the Type II boundary, compositional traces are still evident by differences in etching characteristics. Each SGB represents the boundary between two weld metal grains, therefore, as observed in these figures, the Type II traverses several weld metal grains.

Similar results are shown in Fig. 8, where the transformation product along the cores of the original solidification cell structure delineates two different solidification grains. This is characterized by the difference in angles subtended between each, and normal to the fusion boundary interface, as illustrated in this figure. These results indicate the Type II boundary migrated from the fusion boundary into the weld metal within the austenite temperature regime. Although the crystallographic portion of the SGB has been eliminated by the Type II boundary, there still exists a compositional difference between the matrix and a boundary, whether it is a SGB or a solidification subgrain boundary. This produces the differential etching between matrix and grain boundary or prior grain boundary and martensite along cell cores as has been shown in Fig. 8.

Although it is difficult to locate a specific boundary in a TEM foil, with the assistance of OIM analysis and careful ion milling, several Type II boundaries were located and analyzed. Intersection of a Type II and solidification grain boundary, shown in Fig. 9, was observed in a 48% BMD weld (same sample used for OIM analysis). The Type II boundary exhibits no particular details that would distinguish it from any other grain boundary in the weld metal, other than it is oriented roughly perpendicular to SGBs in the weld metal. However, it is interesting to note the discontinuity of the Type II boundaries when they intersect SGBs. This feature was observed in many of the optical and TEM photomicrographs.

Despite the analysis above, this does not present any statistical basis for generalizing all orientation relationships along the fusion boundary. The possible grain boundary pairs/misorientations along any given fusion boundary are numerous. To determine any statistically preferred misorientations at the fusion boundary using TEM poses a daunting, if not impossible, task. Therefore, OIM analyses were employed as a more efficient means to obtain and evaluate grain boundary information along the fusion boundary.

Several samples were analyzed by OIM to evaluate larger regions of the fusion boundary. Although very useful, OIM could not be performed on all samples by virtue of the ability to resolve individual backscatter patterns from very fine structures, *i.e.,* martensite. Therefore, it was not possible to perform this analysis on those samples where martensite was prominent along the fusion boundary.

The OIM results obtained from welds produced at 48% BMD, which exhibits a fully austenitic weld metal microstructure, are shown in Figs. 10–12. A representative grain map reproduced from data collected over a region approximately 1440 x 1525 μm with a step size increment of 5 μm is shown in Fig. 10. Grain maps are similar to a photomicrograph of a polished and etched sample; however, large and small angle grain boundaries are delineated in the OIM map by the thickness of the lines. Lighter lines represent misorientations between 5 and 15 deg, and heavier lines represent misorientation greater than 15 deg. Once drawn, these maps provide an interactive tool for extracting various lattice and grain boundary information from locations of interest. For this investigation, regions of interest include the fusion boundary and Type II boundaries.

Intensity plots of misorientations gen-

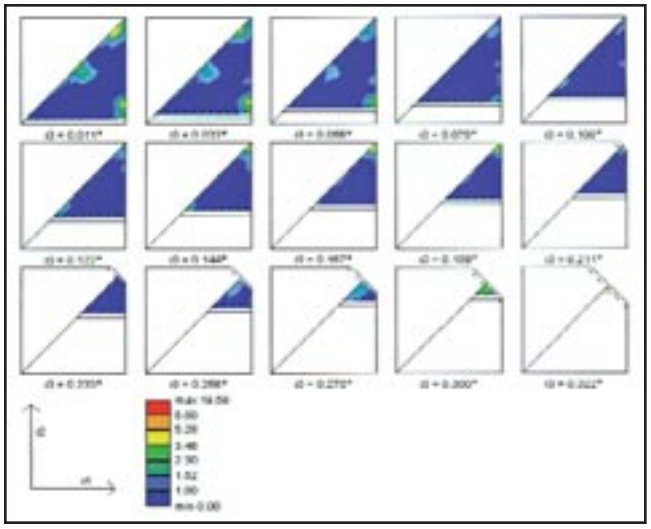

*Fig. 11 — Misorientation results of entire region plotted in Rodrigues Space (intensity). Note the higher intensities at 27 deg @ [110], 50 deg @ [110], 45 deg @ [100] and 60 deg @ [111] (Σ3).*

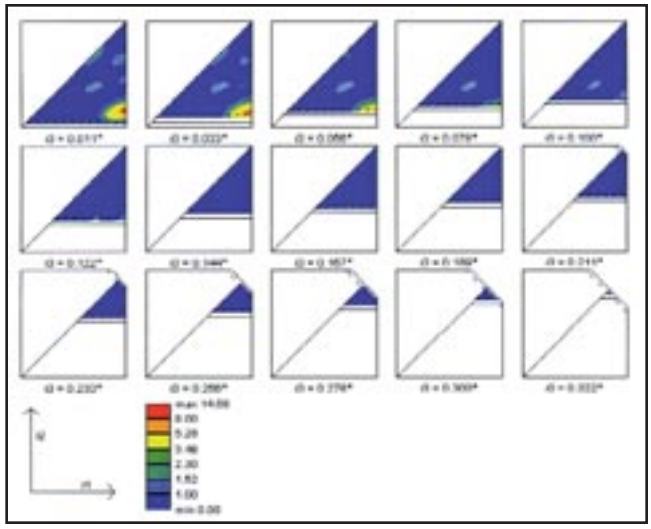

*Fig. 12 — Results of misorientation analysis from Fig. 10 between weld metal and HAZ grain at the fusion boundary. Results indicate tendencies toward 35 deg @ [110] (K-S) and 45 deg @ [100] (Bain).*

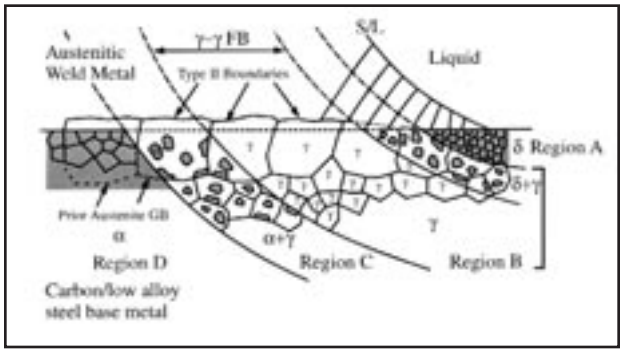


*Fig. 13 — Schematic illustration of fusion boundary microstructural evolution in dissimilar metal welds. The curved lines represent the locus of the transformation temperatures.*

erated from data sets are presented in Rodrigues-Frank space in Figs. 11 and 12. Misorientations of the entire data set exhibit a relatively random distribution of grain boundary misorientations with some higher densities observed toward 45 deg about <100> (lower right corner of $r^3$ = 0.011 plot), 27 deg @ <110>, 45 deg about <110> (upper right corner of $r^3$ = 0.011 plot) and 60 deg @ <111> (upper right hand corner of $r^3$ = 0.300 plot), as shown in the intensity plots in Fig. 11.

Using the grain map in Fig. 10, misorientations between HAZ and weld metal grains at the fusion boundary were analyzed. The highlighted points (indicated in yellow) in Fig. 10 represent those locations at which individual misorientation data were taken. Misorientation distributions were calculated from these data and plotted in Rodrigues-Frank space as intensity plots. This plot shows tendencies toward 35 deg @ <110> and 45 deg @ <100> indicated by the increase in intensity at the upper right-hand corner along the diagonal (<110>), and at the lower right-hand corner of plots $r^3$ = 0.011–0.056, respectively, in Fig. 12.

As various orientation relationships may be represented in Rodrigues-Frank space, it is important to point out those of particular interest to the present investigation. As the angle/axis pairs for the Bain, K-S and N-W orientation relationships are approximately 45 deg @<100>, 35 deg @<110> and 45 deg @<110>, respectively, these correspond directly to locations within the Rodrigues-Frank space plots. As the diagonal in $r^3$=0.011 represents the <110> rotation axis, the K-S and N-W orientation relationships would lie at roughly 35 and 45 deg toward the upper right-hand corner along this axis. Likewise, the horizontal line in this plot corresponds to the <100> rotation axis, and the Bain orientation relationship lies at the lower right-hand corner, *i.e.,* 45 deg @<100>. Therefore, the stronger tendency exhibited in Fig. 12 would be toward the Bain orientation relationship, indicated by the higher intensity. This same trend was observed in several other samples of different BMDs.

## Discussion

In similar metal welds, growth of the solid in the molten weld pool is initiated by arranging atoms in the liquid phase on the existing crystalline substrate, thereby extending it without altering the crystallographic orientation (Refs. 22–24). As a result, misorientations between adjacent HAZ grains are continuous across the fusion boundary into the weld metal, creating solidification grain boundaries (SGBs) as solidification proceeds. Thus, there is no crystallographic misorientation between a weld metal grain and the HAZ grain from which it grew, producing a cube-on-cube relationship, *i.e.,* {100}//{100}, <100>//<100> for cubic materials. In an autogenous weld on high-purity iron, the original solid to form would exhibit this orientation relationship with the HAZ grains from which it grew. However, it becomes increasingly difficult to maintain this relationship as a dissimilar filler metal is introduced, creating differences in composition, lattice parameter, structure, etc., as would be the case in most DMWs

### Nature of the Fusion Boundary within the Austenitic Temperature Range

In a previous paper (Ref. 1), the nature and character of the fusion boundary within the δ-ferrite temperature range was discussed. This paper mainly addressed the nucleation and growth phenomenon during the initial stages of solidification illustrated in region A of Fig. 13. It was proposed that the initial solid forms at the fusion boundary by a heterogeneous nucleation event, a result of differences in composition, lattice parameter and crystal structure between the substrate (BCC) and weld metal (FCC). As these solid nuclei form, they adopt a closest match orientation relationship with the partially melted substrate grains at the

fusion boundary from which they nucleate. As a result, the fusion boundary is no longer a simple transition between wrought and cast material, but is made up of random grain boundary types of large misorientations between HAZ and weld metal grains. The nature of this elevated temperature boundary affects the evolution of the fusion boundary and surrounding microstructure during the on-cooling phase transformation. (Note: for consistency and brevity, in the following discussion the authors will use terminology and symbols consistent with the Fe-C phase diagram when describing the various phases, phase transformation and interphase boundaries in the HAZ; $\delta$ for the elevated temperature BCC iron ferrite; $\gamma$ for FCC iron austenite; and $\alpha$ for the lower temperature BCC iron ferrite. However, when referring to the weld metal, which is a nickel-copper-rich phase, FCC will be used.)

As the weld and surrounding HAZ cool, the $\delta$-$\gamma$ interphase boundary in the HAZ approaches the fusion boundary illustrated in Region B of Fig. 13. In an autogenous weld on iron or steel, the fusion boundary offers little or no resistance to this interphase boundary, as it is simply a change from wrought to cast material. As there is no difference in composition, structure and orientation at the fusion boundary, the $\delta$-$\gamma$ interphase boundary keeps advancing toward the centerline of the weld without hindrance.

However, in a DMW the $\delta$-ferrite in the HAZ does not advance beyond the fusion boundary, as the weld metal is stable FCC. When the $\delta$-$\gamma$ interphase boundary intersects the fusion boundary, the fusion boundary now becomes a metastable $\gamma$-FCC boundary between two phases (HAZ iron-rich austenite and weld metal nickel-copper-rich FCC) of vastly different composition. When this occurs, several questions arise regarding the nature and mobility of this $\gamma$-FCC boundary. These will be discussed below.

In homogenous welds, the weld metal grain size is roughly equivalent to the HAZ grain size adjacent to the fusion boundary. Unlike homogeneous welds, the weld metal grain size in DMWs may be smaller or larger than the HAZ grain size (Ref. 20). Likewise, the austenite in the near HAZ may exhibit a much larger grain size than the $\delta$-ferrite. As a result, when the $\delta$-$\gamma$ boundary reaches the fusion boundary, the larger austenite HAZ grains may traverse several weld metal grains and SGBs.

Not only are the grain sizes different, but the fusion boundary is now made up of numerous grain boundaries of various misorientations between the iron-rich austenitic HAZ and the nickel-rich austenitic weld metal grains. Because solidification of the austenitic weld metal may have initiated heterogeneously, and the austenite grain size in the near HAZ may be quite large, it is likely that the larger austenite grains in the HAZ will traverse more than one weld metal grain and SGBs at the fusion boundary when the $\delta$-$\gamma$ interphase boundary intersects the fusion boundary as illustrated in Region B of Fig. 13. As a result, the fusion boundary becomes an austenite-FCC ($\gamma$-FCC) grain boundary made up of various random misorientations between the austenitic HAZ and weld metal grains. At this point, the fusion boundary is no longer a simple transition between wrought and cast materials, but is a $\gamma$-FCC boundary between the iron-rich HAZ (metastable austenite) and the nickel-rich weld metal grains (stable FCC). When this occurs, growth of the austenite in the HAZ can no longer proceed by transformation, as there is no $\delta$-ferrite present in the fully austenitic weld metal. However, the newly formed $\gamma$-FCC fusion boundary can migrate as a grain boundary under normal grain growth mechanisms.

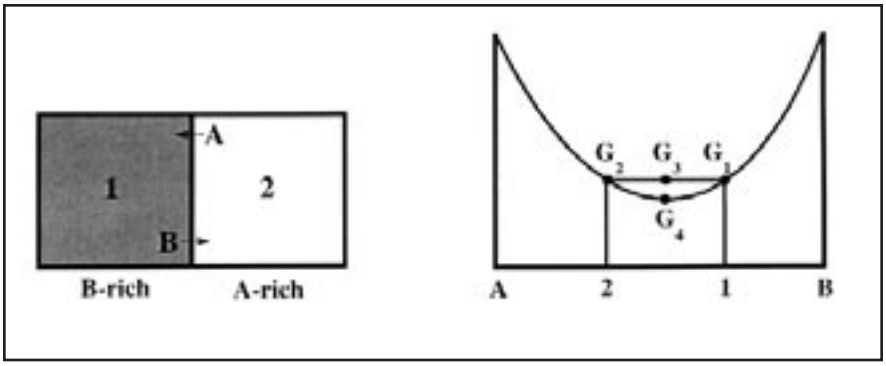


*Fig. 14 — Free energy and chemical potential changes during "downhill" diffusion. A — welded block of different compositions; B — free energy diagram for welded blocks.*

#### Mobility of the Austenite-Austenite Fusion Boundary

The mobility of the $\gamma$-FCC dissimilar boundary, now superimposed on the original fusion boundary, is greatest in the austenite temperature range. This is due to the fact that only short-range diffusion is required for this boundary to migrate. In DMWs, the weld metal has been stabilized by the additions of austenitic stabilizing elements (Ni and Cu) from the filler metal. For the initial $\delta$-ferrite, or the lower temperature $\alpha$-ferrite, to migrate into the weld metal, long-range diffusion would be required to reduce the stability of the FCC weld metal phase for it to be transformed to a BCC ferrite phase. However, long-range diffusion is highly unlikely to occur during the rapid thermal cycles associated with welding. Therefore, the newly formed $\gamma$-FCC dissimilar boundary located at the fusion boundary is most mobile when the fusion boundary region is within the austenitic temperature range because only short-range diffusion is required.

Several factors could affect the mobility of the $\gamma$-FCC dissimilar boundary. These include 1) steep thermal gradient, 2) composition gradient, 3) interfacial strain across the fusion boundary, and 4) elimination of grain boundary area, *i.e.,* solidification grain boundaries (SGBs) or migrated grain boundaries. From a thermodynamic standpoint, the driving force behind the continued migration of the $\gamma$-FCC dissimilar boundary is the reduction in Gibbs free energy. Those elements contributing to an increase in free energy which could be reduced or eliminated by the migration of the $\gamma$-FCC dissimilar boundary include 1) the composition gradient at the fusion boundary, and 2) interfacial strain energy.

Several of the above-mentioned elements have been investigated in various grain growth studies. Yoo, *et al.,* investigated the effects of thermally induced stress/strain on grain growth in Ag (Ref. 25). They observed grain boundary migration distances greater than 40 μm in quenched and annealed Ag samples. They also observed higher heating-rates and annealing temperatures produced greater distances of grain boundary migration. They concluded the thermal strain produced as a result of quenching and rapid heating was sufficient to produce grain boundary migration, similar to strain-induced boundary migration, in mechanically deformed materials. Other investigators have observed similar trends in their studies of strain-induced boundary migration (Ref. 26) and abnor-

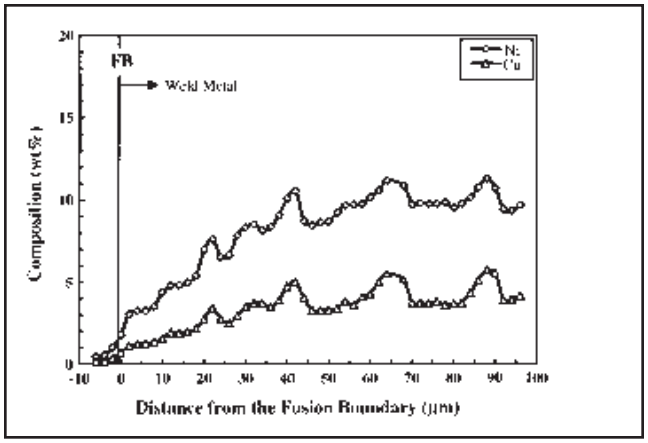


*Fig. 15 — Electron microprobe analysis across the fusion boundary at 80% BMD weld in Fe/70Ni-30Cu. Note that the bulk weld metal dilution is reached within approximately 40 μm of the FB.*

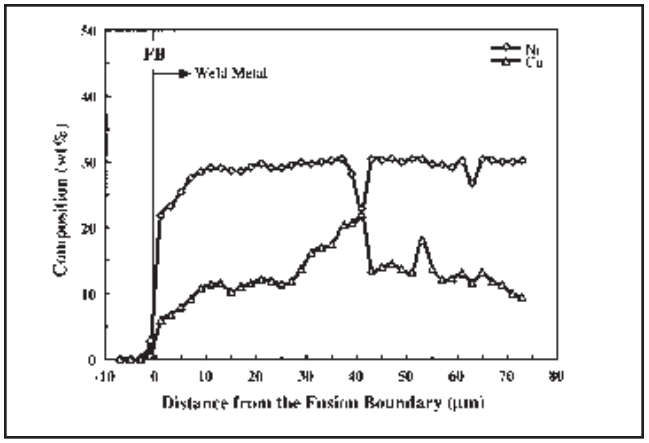


*Fig. 16 — Electron microprobe analysis across the fusion boundary in a 46% BMD weld in Fe/70Ni-30Cu. Note that the bulk weld metal dilution is reached in approximately 10 μm.*

mal grain growth (Refs. 27–29). Randle concluded anomalous grain growth was induced in Ni by the application of 2% pre-strain prior to annealing (Ref. 27). Likewise, Gastaldi, *et al.* (Ref. 28), and Srolovitz, *et al.* (Ref. 29), concluded the driving force for anomalous grain growth is mainly strain related.

The presence of high peak residual stresses in weldments is an accepted and well-known fact associated with welding. This may be compounded with the differences in coefficient of thermal expansion between base and weld metal in DMWs. Schimmoller observed tensile residual stresses in as-welded roll bond clad plate on the order of 20 ksi (Ref. 30). Likewise, Nho, *et al.*, observed peak tensile residual stresses in clad components on the order of 48 ksi in Type 309L clad materials (Ref. 31). Residual stresses of this magnitude are in excess of the yield strength of the Type 309L filler metal, commonly used filler for cladding or DMW. Residual stresses of these magnitudes are typically associated with differential strains, sufficient to augment normal or even anomalous grain growth at elevated temperatures.

Similar arguments can be made regarding the presence of composition gradients and grain boundary area in the weld metal adjacent the fusion boundary in DMWs. The electron microprobe analyses presented in Figs. 15 and 16 demonstrate the composition gradients present at the fusion boundary in DMWs. From a free energy standpoint, it is energetically favorable to homogenize the composition in any system, and minimize the grain boundary area, as both contribute to the total free energy of a system. The reason diffusion occurs is to produce a decrease in Gibbs free energy (Ref. 32). A common example used by many in describing diffusion kinetics is to weld together two blocks of the same A-B solid solution (Fig. 14A), but of different compositions. The welded block is held at an elevated temperature in order for long-range diffusion to occur. This makes a nice illustration, as this is exactly what is attained in DMWs. As BMD decrease, the composition gradient at the fusion boundary becomes very steep as observed in Fig. 16. Considering the molar free energy diagram in Fig. 14B, if the molar free energy of each alloy is represented by $G_1$ and $G_2$, then initially the total free energy of the welded block will be $G_3$. If diffusion occurs as shown in Fig. 14A so as to eliminate the concentration differences, then the total free energy will decrease toward $G_4$, the free energy of a homogeneous alloy. Although there is insufficient time for this to occur in a normal weld thermal cycle, there is a strong driving force for the γ-FCC dissimilar boundary to migrate into the weld metal, as the rate of solute diffusion (especially substitutional solute) across a grain boundary is greater than matrix diffusion (Refs. 32–33). Likewise, the temperature range over which this occurs would be roughly $0.5–0.95T_m$, where boundaries have significant mobility (Ref. 32) and vacancy concentrations are typically very high. Similarly, a reduction in free energy comes from the decrease in total grain boundary area. Therefore, as the γ-FCC dissimilar boundary migrates into the weld metal, those SGBs that initially extended to the fusion boundary would be eliminated, and the total free energy of the system reduced (Refs. 32, 33).

Similar mechanisms have been used to described the theory of diffusion-induced grain boundary migration (DIGM). Several investigations have demonstrated the effects of composition gradients and coherency strain energies as possible driving forces for DIGM (Refs. 34–37). Likewise, elevated temperatures only act to enhance diffusion kinetic of both solute and solvent, thus, amplify DIGM (Ref. 37). It has been shown in the present investigation that many of these characteristics, *i.e.,* composition and strain gradients, are inherent along the fusion boundary in DMWs. Therefore, DIGM poses a viable mechanism for explaining the driving force for the γ-FCC dissimilar boundary to migrate into the weld metal, creating the Type II boundary.

This proposed mechanism of the type II boundary formation described above differs from Wu, *et al*. (Ref. 15), who proposed that the Type II boundary formed during solicitation. They proposed that solidification initiates from the substrate as primary ferrite but after a short distance changes to primary austenite due to the increase in austenitic stabilizing elements in the weld metal, leaving behind a residual high angle grain boundary. The original primary ferrite then transforms to austenite at lower temperature during the on-cooling weld thermal cycle. If this were the case, there should exist some FCC/BCC orientation relationship consistent with FCC/BCC interfacial growth; however, this is not the case. The mechanism proposed in the present paper suggests the Type II boundary is a result of solid-state grain boundary migration in the austenitic temperature range during the on-cooling weld thermal cycle.

#### Summary of the Fusion Boundary within the Austenite Temperature Range

It is likely all of the characteristics discussed above may be present at the fusion boundary in DMWs. Steep thermal

gradients are inherent in a weld thermal cycle as a result of efficient heat extraction by the base metal surrounding the weld. Likewise, steep composition gradients near the fusion boundary exist via diffusional mixing of filler metal alloying elements within the stagnant boundary layer. Strain energy at the fusion boundary is created by a combination of lattice mismatch and differences in coefficient of thermal expansion between base and weld metals. Likewise, the high residual stresses inherent to fusion welding contribute to a significant amount of strain near the fusion boundary. Therefore, it is likely that, within the austenite temperature range, the γ-FCC dissimilar boundary migrates into the weld metal as a result of the strong driving force for grain growth, producing the Type II boundary so often observed in DMWs. It is also possible that one or any combination of these may also contribute to the cracking related problem in DMWs.

#### Nature of the Fusion Boundary within the α-Ferrite Temperature Range

As the gamma-alpha interphase boundary moves through the HAZ toward the fusion boundary, illustrated in Region C and D in Fig. 13, the austenite in the HAZ is transformed to the lower temperature BCC α-ferrite. A detailed understanding of the nucleation and growth of α-ferrite within the austenite is critical in explaining the evolution of the fusion boundary. The orientation relationship observed between the HAZ and weld metal grains at the fusion boundary begins to evolve within the austenite temperature range, as the austenite in the near HAZ grows toward the fusion boundary, consuming the BCC delta-ferrite phase, and into the weld metal.

As the delta-gamma interphase boundary migrates through the HAZ and into the weld metal, it leaves behind a coarse-grain austenite region. Within the austenite temperature range, these coarse austenite grains are able to grow across the fusion boundary and into the weld metal. This morphology is illustrated in Fig. 13 as Region B. At this point, the austenite in the HAZ extends across the fusion boundary, exhibiting a cube-on-cube relationship between the HAZ and weld metal, as they are the same grains. As the weld cools, the lower temperature γ-α interphase boundary in the HAZ moves toward the weld fusion boundary, transforming the higher temperature FCC austenite in the HAZ to the lower temperature BCC α-ferrite.

It is likely the γ-α transformation proceeds by both nucleation and growth. Initially, the existing α-ferrite at the γ-α interphase boundary grows behind the γ-α interphase boundary. The morphology and kinetics of nucleation of α-ferrite in austenite has been well documented (Refs. 32, 33, 38). At higher temperatures, α-ferrite forms at the austenite grain boundaries exhibiting an equiaxed or lenticular morphology. These will often nucleate in an orientation so as to minimize the energy of the interface between ferrite and austenite (Ref. 33). This is often accomplished by having a well-defined orientation with one grain while exhibiting an arbitrary orientation with the opposing grain. One of the best defined orientation relationships observed between α-ferrite and austenite is that of Kurdjumov-Sachs (K-S). As the temperature of transformation decreases, these crystals develop facets on at least one side, but often on both. Other morphologies include 1) Widmanstätten sideplates or laths, 2) intragranular blocky ferrite, and 3) intragranular plates. The two latter morphologies nucleate within the austenite grains.

It is likely that several of these morphologies may be present in the various regions of the HAZ. From the micrographs evaluated, it appears the predominate morphology is intragranular ferrite, giving rise to the equiaxed morphology observed in the HAZ microstructure, especially in the near HAZ. However, the presence of some facets or sideplates was evident in many of the HAZ microstructures. The intragranular morphology is characteristic of a larger austenite grain size. In fine-grain samples, essentially all the nuclei will form at, and grow from, the austenite grain boundaries. In a coarse-grained material, the grain boundaries will be covered by nuclei early in the transformation, but ultimately nuclei will form inside the grain to reduce the supersaturation within the grain (Ref. 33).

During a weld thermal cycle, those austenite grains adjacent the δ-γ interphase boundary will have experienced the longest time and the highest peak temperature within the austenite temperature range. As a result, this region will exhibit the largest austenite grain size, Region B in Fig. 13. As the γ-α interphase boundary moves through the austenite in the near HAZ, initially the α-ferrite will form at the austenite grain boundaries. However, because of the large austenite grain size, α-ferrite will also nucleate intragranularly, producing the equiaxed α-ferrite morphologies observed. The manner in which this nucleation occurs gives rise to the various fusion boundary orientation relationships observed in the present investigation.

Similar to grain boundary allotriomorphs, intragranular nuclei will nucleate in specific orientations so as to minimize the interfacial energy between austenite and ferrite. The typical orientation relationships observed between FCC and BCC materials include 1) the Bain, 2) the Kurdjumov-Sachs, and 3) the Nishyama-Wassermann relationships. The α-ferrite that nucleates and grows within the coarse austenite grains adjacent the fusion boundary will nucleate with one of these specific orientation relationships. Once nucleated, the ferrite nuclei will continue to grow until all the austenite in the HAZ has been transformed. Although the gamma-alpha interphase isotherm will continue toward the weld centerline as the weld cools, growth of the α-ferrite in the near HAZ will terminate at the fusion boundary because the weld metal is stable FCC to below room temperature as a result of alloying from filler metal additions.

The fusion boundary orientation relationships observed in DMWs in the present investigation are a result of abnormal austenite grain growth, followed by nucleation and growth of α-ferrite grains on specific orientations within these coarse austenite grains. Because the coarse prior austenite grains in the HAZ were able to migrate across the fusion boundary, the crystallographic orientation is not altered at the fusion boundary, even though the composition changes dramatically. Therefore, any α-ferrite that nucleates within these HAZ austenite grains would exhibit the same orientation relationship with that portion of the austenite grain extending into the weld metal. Evidence of this was presented in a previous paper by Nelson, *et al*. (Ref. 21), where TEM analyses demonstrated the relationship between base (BCC) and weld (FCC) metal exhibited a Nishyama-Wassermann orientation relationship. Likewise, similar trends were presented in the OIM misorientation analyses (Fig. 12) where the orientation relationships at the fusion boundary tend toward those common FCC/BCC relationships: the Kurdjumov-Sachs, Nishyama-Wassermann, and Bain relationships.

#### Summary on the Nature of the Fusion Boundary in Dissimilar Metal Welds

As a result of the inherent differences between base and weld metal in DMWs, the evolution of the fusion boundary microstructure and orientation relationships is complex. Within the δ-ferrite temperature range, the fusion boundary exhibits various grain boundary misorientations that may or may not include those orientation relationships characteristic of FCC/BCC interfaces. Within the

austenite temperature range, the δ-γ interphase boundary moves through the HAZ toward the fusion boundary. As this occurs, the coarse austenite grains in the HAZ intersect the fusion boundary, creating a γ-FCC dissimilar boundary between HAZ and weld metal. As a result of the large austenite grain size, the HAZ grains may traverse several weld metal grains and SGBs, creating a fusion boundary of various misorientations. However, because both the HAZ and weld metal are austenite when the HAZ is in the austenite temperature range, the γ-FCC dissimilar boundary at the fusion boundary is rendered mobile.

As the weld cools through the austenite temperature range the γ-FCC dissimilar boundary migrates into the weld metal. The driving force behind the migrating γ-FCC boundary is the reduction in free energy. Inherent differences between base and weld metals in DMWs create steep composition gradients adjacent the fusion boundary in the weld metal, and interfacial strain across the fusion boundary. As the γ-FCC dissimilar boundary migrates across the transition region in the weld metal, these factors may be reduced or eliminated, thereby reducing the free energy of the system. The composition becomes more homogenous by diffusion across and along the γ-FCC dissimilar boundary as it migrates through the transition region. This migrating boundary may sweep or carry iron into the weld metal while at the same time allowing Ni and Cu to diffuse across or along it toward the base metal. All of these factors contribute to the driving force for the γ-FCC dissimilar boundary to migrate into the weld metal.

At lower temperatures, the γ-α interphase boundary eventually intersects the fusion boundary. In the near HAZ where the austenite grain size grew quite large, α-ferrite nucleates at austenite grain boundaries and as intragranular idiomorphs. The α-ferrite nuclei continue to grow toward the fusion boundary behind the gamma-alpha interphase boundary, eventually consuming all austenite in the HAZ. However, growth of the α-ferrite is interrupted at the fusion boundary, as the composition of the weld metal no longer supports the gamma-alpha transformation. For the α-ferrite to grow into the weld metal, long-range diffusion of substitutional alloying elements would be required to decrease the stability of the austenitic weld metal. Over the short diffusion times created by the rapid thermal cycles associated with welding, this will not occur.

The orientation relationships observed between the HAZ α-ferrite and the austenitic weld metal result from the fact the habit planes on which the α-ferrite nucleate are continuous across the fusion boundary. This occurred when the coarse-grain austenite grains in the HAZ grow behind the advancing γ-FCC dissimilar boundary, across the fusion boundary and into the weld metal. As a result, a cube-on-cube relationship was created between base and weld metal within the austenite temperature range. The lower temperature α-ferrite then nucleated within these large austenite grains and grew up to the fusion boundary. Although the growth of these grains was terminated at the fusion boundary, they share the same orientation relationship with the weld metal grains as they did with the prior austenite HAZ grains adjacent the fusion boundary. This gives rise to those misorientation trends observed between HAZ and weld metal grains, as shown in Figs. 11 and 12. As a result, the fusion boundary exhibits large misorientations (>15 deg) rather than the small misorientation observed in homogeneous welds (<5 deg).

## Conclusions

From the results and discussion presented, the following conclusions can be made:

1) The Type II boundary forms from the elevated temperature γ-FCC boundary that is present along fusion boundary in dissimilar metal (FCC/BCC) welds.

2) Fusion boundary orientation relationships between adjacent HAZ and Type II grains show trends toward the Bain relationship in the present $Fe_{BM}$/$Ni\text{-}Cu_{WM}$ system.

3) Based on the results of this investigation the authors can explain the formation of the Type II boundary and resulting fusion boundary orientation relationships observed by proposing the following model:

The formation of the Type II boundary is dependent on the solidification behavior of the weld metal and the nature of solid-state transformations in the base metal substrate. The occurrence of the allotropic δ-γ transformation at elevated temperature is thought to be necessary to produce a Type II boundary. In those base metals that undergo a δ-γ transformation, the fusion boundary becomes a γ-FCC grain boundary of various misorientation between base (Fe austenite) and weld (Ni-Cu-rich FCC) metals within the austenitic temperature range. As both base and weld metals are austenite of similar lattice parameters, this boundary is mobile by short range diffusion across the grain boundary interface. Within the austenite temperature range, the γ-FCC dissimilar boundary migrates into the weld metal as a result of a strong driving force. The driving forces promoting this migration include 1) steep temperature gradient, 2) composition gradient, and 3) strain energy produced by differences in lattice parameter and coefficient of thermal expansion, and non-equilibrium cooling associated with welding.

The room temperature fusion boundary orientation relationships observed in DMWs is dependent upon the nature of the fusion boundary within the austenite temperature range 1) if the γ-FCC fusion boundary is mobile and migrates into the weld metal within the austenite temperature range, nucleation of α-ferrite within the coarse austenitic HAZ grains with specific crystallographic relationships, these same orientations will occur along the fusion boundary between base and weld metal grains; and 2) if the fusion boundary is immobile, the room temperature fusion boundary will exhibit various random misorientations between HAZ grains and the austenitic weld metal grains.

*Acknowledgments*

This work was supported by Dr. John C. Lippold at The Ohio State University. The authors wish to thank INCO Alloys for providing the filler metal used in this investigation. Technical support provided by the Welding and Joining Metallurgy Group at The Ohio State University was greatly appreciated.

*References*

1. Nelson, T. W., Lippold, J. C., and Mills, M. J. 1999. Nature and evolution of the fusion boundary in ferritic-austenitic dissimilar weld metals, part 1 — nucleation and growth. *Welding Journal* 78(10): 329-s to 337-s.

2. Matsuda, F., and Nakagawa, H. 1984. Simulation test of disbonding between 2.25%Cr-1%Mo steel and overlaid austenitic stainless steel by electrolytic hydrogen charging technique. *Transactions of JWRI*, 13(1):159–161.

3. Sakai, T., Asami, K., Katsumata, M., Takada, H., and Tanaka, O. 1982. Hydrogen induced disbonding of weld overlay in pressure vessels and its prevention. *Current Solutions to Hydrogen Problems in Steels*. Proceedings, 1st International Conference, Washington, D.C., pp. 340–348. Eds: C. G. Interrante and G. M. Pressouyre, ASM International, Materials Park, Ohio, ISBN 0-87170-148-0.

4. Hattori, T., Fujita, T., Kinoshita, K., Ebata, A., Tsukamoto, H., and Ando, M. 1986. Hydrogen induced disbonding of stainless steel overlay weld and its preventive measures. *Nippon Kokan Technical Report Overseas*, No. 47. pp.17–22.

5. Kinoshita, K., Itoh, H., Ebata, A.,

and Hattori, T. 1985. Microscopical critical condition for the initiation of disbonding of weld overlaid pressure vessel steel. *Transactions of the Iron and Steel Institute of Japan* 25(6): 505–512.

6. Ohnishi, K., Fuji, A., Chiba, R., Adachi, T., Naitoh, K., and Okada, H. 1984. Study on a stainless steel overlay welding process for superior resistance to disbonding. report 1: effect of strip overlay welding conditions on resistance to hydrogen-induced disbonding. *Transactions of the Japan Welding Society* 15(2): 129–135.

7. Matsuda, F., *et al*. 1984. Disbonding between 2.25%Cr-1%Mo steel and overlaid austenitic stainless steel by means of electrolytic hydrogen charging technique. *Trans. JWRI*, 13(2): 263–272.

8. Matsuda, F., Nakagawa, H., and Tsuruta, S. 1986. Proposal of hydrogen blistering mechanism associated with disbonding between 2.25%Cr-1%Mo steel and Type 309 (stainless steel) overlaid metal. *Transactions of JWRI*, 15(2): 207–208.

9. Morishige, N., Kume, R., and Okabayashi, H. 1985. Influence of low-temperature hydrogen degassing on hydrogen-induced disbonding of cladding. *Transactions of the Japan Welding Society* 16(1): 12–18.

10. Blondeau, R., Pressouyre, G. M., Cheviet, A., Berthet, J. A., and Duranseaud, J. M. 1982. Contribution to a solution to the disbonding problem in 2.25%Cr-1%Mo heavy wall reactors. *Current Solutions to Hydrogen Problems in Steels.* pp. 356–360. Proceedings, 1st International Conference, Washington, D.C., Eds., C. G. Interrante and G. M. Pressouyre. ASM International, Materials Park, Ohio, ISBN 0-87170-148-0.

11. Pressouyre, G. M., Chaillet, J. M., and Valette, G. 1982. Parameters affecting the hydrogen disbonding of austenitic stainless cladded steels. *Current Solutions to Hydrogen Problems in Steels.* pp. 349–355, Proceedings, 1st International Conference, Washington, D.C., Eds. C. G. Interrante and G. M. Pressouyre, ASM International, Materials Park, Ohio, ISBN 0-87170-148-0.

12. Frederick, G., and Hernalsteen, P. 1981. Underclad cracking in PWR (pressurized water reactor) reactor vessels. Translation CE 7892, London, England, Central Electricity Generating Board, Translations Section, pp. 22 (Translation of Paper 20 presented at AIM Meeting, Modern Electric Power Stations, Liege, Belgium, 1981).

13. Horiya, T., Taeda, T., and Yamato, K. 1985. Study on underclad cracking in nuclear reactor vessel steels. Transactions of the ASME, *Journal of Pressure Vessel Technology* 107(1): 30–35.

14. Thielsch, H. 1952. Stainless steel weld deposits on mild and alloy steels. *Welding Journal* 31(1): 37-s to 64-s.

15. Lundin, C. D. 1982. Dissimilar metal welds-transition joints literature review. *Welding Journal* 61(2): 58-s to 63-s.

16. Wu, Y., and Patchett, B. M. 1992. Formation of crack-susceptible structures of weld overlay of corrosion resistant alloys. pp. 206–219, *31st Metallurgist Conference of CIM*, Edmonton, Canada.

17. Edington, J. W. 1976. *Practical Electron Microscopy in Materials Science,* reprinted by TechBooks, Herndon, Va.

18. Adams, B. L. 1993. Orientation imaging microscopy: application to the measurement of grain boundary structure. *Materials Science and Engineering*, A166, pp. 59–66.

19. Wright, S. I. 1993. A review of automated orientation imaging microscopy (OIM). *Journal of Computer-Assisted Microscopy* 5(3): 207–221.

20. Adams, B. L., Wright, S. I., and Karsten, K. 1993. Orientation imaging: the emergence of a new microscopy. *Met. Trans. A*, 24A, pp. 819–831.

21. Nelson, T. W., Lippold, J. C., and Mills, M. J. 1998. Investigation of boundaries and structures in dissimilar metal welds. *Science and Technology of Welding and Joining* 3(5): 249–255.

22. Flemings, M. C. 1974. *Solidification Processing.* McGraw-Hill Publishing Co.

23. Savage, W. F., and Aronson, A. H. 1966. Preferred orientation in the weld fusion zone. *Welding Journal* 45(2): 85-s to 89-s.

24. Samuel, J. 1979. Crystallography in fusion-weld-metal solidification mechanics. Ph.D. Dissertation, Rensselaer Polytechnic Institute, Troy, N.Y.

25. You, C-Y., Han, S-C., and Yoon, D-K. 1995. The grain boundary migration in Ag induced by thermal strain. *Metallurgical and Materials Transaction A*, Vol. 26A, pp. 3048–3049.

26. Bailey, J., and Hirsch, P. *Proceedings of the Royal Society,* A267, 11.

27. Randle, V. 1993. Microtexture investigation of the relationship between strain and anomalous grain growth. *Philosophical Magazine A* 67(6): 1301–1313.

28. Gastaldi, J., Jourdan, C., and Grange, G. 1992. *Materials Science Forum*, pp. 94–95, 17.

29. Srolovitz, D. J., Grest, G. S., and Anserson, M. P. 1985. Computer simulation of grain growth, A, abnormal grain growth. *Acta Metallurgica* 33(12): 2233–2247.

30. Schimmoller, H. 1972. Determintation of tensile stresses in evenly plated materials, part 2, tension in warm-rolled, explosion clad austenitic plated steels. *Materials Testing* 14(11): 380–387.

31. Nho, S-H., Ann, H-S., and Ong, C-W. 1992. Derivation of theoretical residual stress and stress intensity factors in dissimilar weld metal of nuclear vessel. pp. 117–123. *Proceedings of an International Conference on Trends in Welding Research,* Gatlinburg, Tenn.

32. Porter, D. A., and Easterling, K. E. 1981. *Phase Transformations in Metals and Alloys.* Published by Van Nostrand Reinhold International, Berkshire, England.

33. Shewmon, P. G. 1983. *Transformations in Metals.* J. Williams Book Co., Jenks, Okla.

34. Shewmon, P. G., and Meyrick, G. 1986. *The Diversity of DIGM (Diffusion Induced Grain Boundary Migration)*, pp. 7–17, ASM International, Materials Park, Ohio.

35. Guan, Z.M., Liu, G.X., Williams, D.B., and Notis, M.R. 1989. Diffusion-induced grain boundary migration and associated concentration profiles in a Cu-Zn alloy. *Acta Metall.* 37(2): 519–527.

36. Rabkin, E. 1994. Gradient and coherency strain energies as driving forces for DIGM. *Scr. Metall. Mater*. 30(11): 1443–1448.

37. Rabkin, E., Shvindlerman, L.S., and Gust, W. 1993. Theory of grain boundary motion during high-temperature DIGM. *Interface Sci.* (Netherlands), 1(2): 133–137.

38. Honeycombe, R. W. K. 1981. *Steels — Microstructure and Properties*. Edward Arnold Ltd., London, U.K.